Adam M. Booth · John Dehls · Trond Eiken · Luzia Fischer · Reginald L. Hermanns · Thierry Oppikofer

Integrating diverse geologic and geodetic observations to determine failure mechanisms and deformation rates across a large bedrock landslide complex: the Osmundneset landslide, Sogn og Fjordane, Norway

Abstract Catastrophic rock avalanches contribute to rapid landscape evolution and can harm humans directly or by secondary effects such as displacement waves. Predicting the volume, timing, and consequences of rock slope failures is therefore essential to managing risk and interpreting landscape response to climatic or tectonic forcing. Here, we synthesize geologic and geodetic observations to document the spatial pattern of movement rates and failure mechanisms at a landslide complex in western Norway, recently identified with systematic interferometric synthetic aperture radar (InSAR) reconnaissance. A differential global navigation satellite system (dGNSS) and global positioning system (dGPS) campaign confirms active slope deformation with horizontal displacement rates of 1.2 to 2.6 mm year^{-1} at four points distributed across the landslide's ~1.8-km width. Displacement vectors are consistent with landslide movement occurring on pre-existing discontinuity sets, and a broad synform controls failure mechanisms within the landslide complex. Two ~1.5 million m³ blocks are wedge failures, while flexural toppling and planar sliding of smaller blocks occur throughout the landslide complex. Modern movement rates are comparable to or slower than Holocene-averaged displacement rates, suggesting continued steady deformation or stabilization of parts of the landslide with time. However, a large volume failure with typical run-out for rock avalanches would likely reach the subjacent fjord, causing a displacement wave. We suggest that our collaborative approach of integrating a wide variety of geologic and geodetic methods will be useful for more thoroughly documenting additional landslide sites and for making informed decisions about risk management.

Keywords Rock slope stability · Bedrock landslide · InSAR · Terrestrial laser scanning · LiDAR · Osmundneset

Introduction

Most of the world's high-relief mountain ranges produce catastrophic rock avalanches, which contribute to rapid landscape evolution by instantaneously denuding bedrock slopes, and can dam rivers or cause displacement waves in standing bodies of water (Whitehouse 1983; Evans and Clague 1988; Schuster et al. 1992; Evans and DeGraff 2002; Korup et al. 2007, 2010; Hewitt et al. 2008; Evans et al. 2011). From a hazard perspective, these secondary and far reaching effects can be more damaging than the rock avalanche itself (Jørstad 1968; Hendron and Patton 1987; Evans 1989; Braathen et al. 2004; Hermanns et al. 2004; Blikra et al. 2005; Bornhold et al. 2007; Redfield and Osmundsen 2009; Kremer et al. 2014). Furthermore, rock avalanche source areas often produce multiple events ranging from minor rock falls to additional rock

avalanches, indicating that their contribution to landscape evolution as well as the hazard they present can persist long after a single event (Plafker and Ericksen 1978; Grimstad and Nesdal 1990; McSaveney 2002; Hermanns et al. 2006; Hewitt et al. 2008).

Improving our ability to predict the timing, volume, and consequences of rock avalanches is essential to managing risk and interpreting landscape response to climatic or tectonic forcing. Making predictions requires recognizing, thoroughly characterizing, and monitoring potential rock avalanche sites, since many source areas show signs of accelerating movement over hours to months before failing catastrophically (Voight 1989; Crosta and Agliardi 2003; Kilburn and Petley 2003; Sartori et al. 2003). With or without a specific trigger, such as an earthquake or hydrologic event, pre-existing geologic structures often control the geometry and deformation of rock slope instabilities (Cruden 1976; Norrish and Wyllie 1996; Hermanns and Strecker 1999; Brideau et al. 2005, 2006; Ganerød et al. 2008; Jaboyedoff et al. 2011a, b; Saintot et al. 2012). In this study, we therefore focus on thoroughly documenting these inherited structures and linking them to rock slope deformation rates at a ~1.8-km-wide bedrock landslide complex in western Norway. To accomplish this goal, we integrate a diverse set of geologic and geodetic observations from fieldwork, interferometric synthetic aperture radar (InSAR), differential global navigation satellite system (dGNSS) and global positioning system (dGPS) measurements, and terrestrial and airborne laser scanning.

The steep, recently deglaciated and debuttressed, crystalline bedrock slopes of western Norway's inner fjord areas are especially prone to catastrophic rock avalanches, often with fatal consequences (Bjerrum and Jørstad 1968; Braathen et al. 2004; Blikra et al. 2006). Our study area, the Osmundneset landslide complex (Fig. 1), lies in the heart of this region in Sogn og Fjordane county, which historically has had at least 179 casualties due to rock avalanches and subsequent processes including displacement waves (Høst 2006). The county therefore has been the subject of an intense mapping and monitoring program carried out by the Geological Survey of Norway (Norges Geologiske Undersøkelse, NGU) since 2007 (Henderson et al. 2008; Hermanns et al. 2011, 2013a). As part of this campaign, we first discovered the Osmundneset landslide complex by systematic regional reconnaissance with interferometric synthetic aperture radar (InSAR), and this study documents the failure mechanisms, rates of movement, and potential for continued activity across the landslide complex. We first measure rates and directions of movement across the landslide complex with InSAR and dGNSS/dGPS, then carry out kinematic feasibility tests for the failure mechanisms based on extensive structural data from field and terrestrial laser scanning

measurements. We combine this geologic data with airborne light detection and ranging (LiDAR) to estimate the volumes of major landslide blocks and to develop a spatial model for the failure mechanism at different locations within the landslide complex. Last, we qualitatively discuss the hazard and risk associated with future movements of the landslide complex.

Study area: the Osmundneset landslide complex

The Osmundneset landslide complex is located on the eastern side of Hyenfjord, a southern branch of Nordfjord, northern Sogn og Fjordane County, Norway (Fig. 1). Its prominent main scarp extends ~1.8 km along the lip of the fjord valley at an elevation of ~1,100 m above sea level and delineates the upslope extent of the landslide complex. Two large, distinct blocks, both with horizontal dimensions of ~200×300 m, are located below this scarp, one near

the scarp's northern end (Fig. 1c, e; point HY-4) and the other near its center (Fig. 1c, d; point HY-3). The ground downslope and to the south of the central block is pervasively cracked and disturbed over an area of ~200×600 m extending to the southern end of the main scarp (Fig. 1c, points HY-1 and HY-2). Despite these widespread signs of deformation on the rock slope, the bathymetry of the subjacent fjord shows no signs of post-glacial rock avalanche deposits, suggesting that the landslide complex has not yet failed catastrophically (Hermanns et al. 2011).

The bedrock underlying the site (Bryhni 2000) consists of the metamorphosed sedimentary rocks of the Neoproterozoic Lykkjebø group (Fig. 1c). Within this group, mica gneiss is found in the stable terrain immediately northeast of the landslide complex. Quartzite and quartz schist crop out in a narrow band below the mica gneiss that parallels the main scarp of the landslide complex such that the
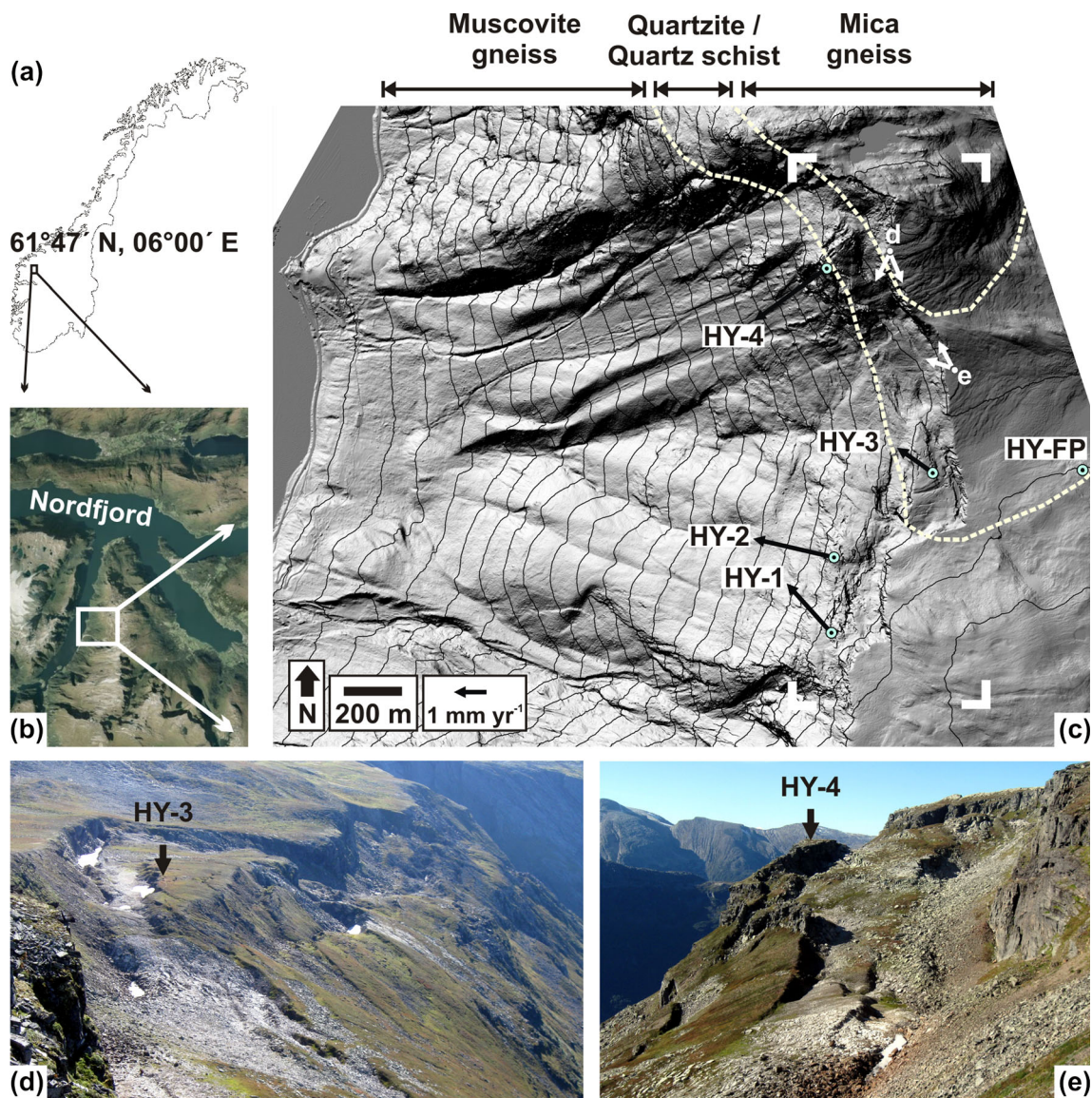

Fig. 1 Overview maps (**a–c**) and photos (**d–e**) documenting the Osmundneset landslide complex, western Norway. Panel (**c**) is a 1-m airborne LiDAR-derived hillshade map overlain with 50-m contours. The *dashed white lines* approximately delineate boundaries between the main lithologies present at the site listed above the figure. Points HY-1 through HY-4 and HY-FP are the locations of dGNSS/dGPS monitoring points, and *black arrows* are their mean velocity vectors from 2008 to 2012. The *white corner brackets* indicate the extent of Fig. 2

two main blocks occur in this bedrock unit. Bedrock is muscovite gneiss on the slope below and to the south of the main blocks of the landslide complex, where the pervasively cracked ground is located and in most of the surrounding area. All three of these units are foliated, and this foliation forms a broad synform with its axis running approximately east–west through the center of the landslide complex. Foliation in combination with other inherited tectonic discontinuities such as faults and fractures accommodates gravitational deformation at sites throughout western Norway (Braathen et al. 2004; Ganerød et al. 2008; Oppikofer et al. 2009, 2011; Böhme et al. 2011; Henderson and Saintot 2011; Jaboyedoff et al. 2011b; Saintot et al. 2011, 2012). "Structural measurements and kinematic analysis" will show how the spatial variation in foliation and fracture orientations exerts a fundamental control on the failure mechanisms at different locations within the landslide complex.

Methods

Interferometric synthetic aperture radar

Our systematic mapping of active landslides throughout western Norway using InSAR first discovered the actively deforming Osmundneset bedrock landslide complex (Hermanns et al. 2011). In this study, we have used four stacks of radar images. Three overlapping sets of ERS-1 and ERS-2 scenes were collected between 1992 and 2000 (track 237, 32 images; track 008, 41 images; track 280, 33 images). One set of 21 Radarsat-2 fine-mode scenes was collected between 2010 and 2013. We analyzed each of these data sets independently to generate four separate line of sight deformation fields. The data were processed using a small baseline subset (SBAS) algorithm implemented in the GSAR software package (Larsen et al. 2006; Lauknes et al. 2011).

The Radarsat-2 images have an average incidence angle of 30° from vertical. The three overlapping ERS data sets are from parallel orbits. Although they all have an average incidence angle of 23° from vertical, this angle varies from near-range to far-range. Thus, the line of site between the satellite and the Osmundneset site varies between the three data sets.

Differential global navigation satellite system and global positioning system

To further constrain movement vectors at the Osmundneset site, we undertook a differential GNSS and GPS campaign beginning in 2008. By physically attaching threaded screws to the bedrock, we installed a network of four roving points spaced throughout the landslide complex as well as one fixed point on stable ground ~400 m to the east of the landslide (Fig. 1c). GNSS receivers (Topcon dual frequency) were used to measure the coordinates of the points on a yearly basis using the Russian Global Navigation Satellite System (GLONASS) and Global Positioning System (GPS) satellites. We left the receivers in place at the network of roving and fixed points for at least 30 min, which resulted in 3σ (99 % confidence) location uncertainties of better than 2 mm for the horizontal coordinates and 4 mm for the vertical coordinates. These uncertainties refer to the internal precision of the measurements within the five-point network rather than to the absolute locations of the points. Measurements were taken once per year during the summer field season, and we report total displacements from 2008 to 2012, which allowed us to most confidently determine displacement vectors averaged over this 4-year time window.

Terrestrial laser scanning and field measurements

To constrain the possible mechanisms that could accommodate movement at the site, we measured the orientations of rock structures using traditional field measurements and terrestrial laser scanning (TLS). Approximately 400 spot measurements of joint and foliation orientations were made throughout the landslide complex at accessible locations from 2008 to 2010. Using TLS-generated point clouds, we made approximately 400 additional structural measurements (Fig. 2) (e.g., Feng and Röshoff 2004; Abellán et al. 2006; Ferrero et al. 2009; Oppikofer et al. 2009, 2011; Sturzenegger and Stead 2009a, b).

TLS data were collected at the southern part of the landslide complex on 23–24 August 2010 and the northern part of the landslide on 5 September 2010 using an Optech ILRIS-3D terrestrial laser scanner. We collected 19 scans from 6 locations distributed throughout the landslide complex (Fig. 2) in order to cover the majority of the exposed rock faces. Point spacing averaged 68 mm at a mean distance of 350 m for the northern part of the landslide and averaged 44 mm at a mean distance of 130 m for the southern part. We aligned individual scans using PolyWorks IMAlign commercial software produced by InnovMetric Software, Inc. This procedure involves generating a mesh from each point cloud, then manually aligning overlapping portions of the meshes and utilizing the program's iterative scheme to minimize the misfit among the overlapping parts of all meshes. We set the grid spacing of the meshes approximately equal to the mean point spacing for each scan, then progressively decreased the maximum search distance for determining the misfit between meshes until doing so no longer improved the quality of the alignment. At the northern site, the largest standard deviation of the misfit between points in overlapping scans was 18 mm, while at the southern site, it was 22 mm. Since these standard deviations arise from differences between points measured on the same surfaces from different scan locations, they provide a good estimate of the maximum relative uncertainty in the location of each point in the final point cloud.

To measure structural orientations, we first georeferenced the TLS point cloud to handheld GPS measurements of the six scan locations. The maximum absolute distance between the scanner positions and GPS coordinates was ~3 m, which is comparable to the uncertainty of the handheld GPS measurements. We then fit planes to clusters of points on exposed joint and foliation surfaces in the point cloud and recorded their orientations in a manner similar to the hand measurements. These structural measurements were used to conduct kinematic feasibility tests for planar sliding, wedge sliding, and toppling at locations throughout the landslide complex.

Surface feature mapping

We created a high-resolution (~1-m spatial resolution) geomorphic map of linear surface cracks, scarps, trenches, and depressions in order to evaluate the abundances and orientations of these features at different locations in the landslide complex. The map is based primarily on the 1-m digital elevation model (DEM) derived from airborne LiDAR in 2010, but supplemented with the aerial photo interpretation, field photographs, and TLS point cloud data where possible (Fig. 2). Linear features visible in the airborne LiDAR were included in the map only if they were also visible in at least one additional data source. Although this map
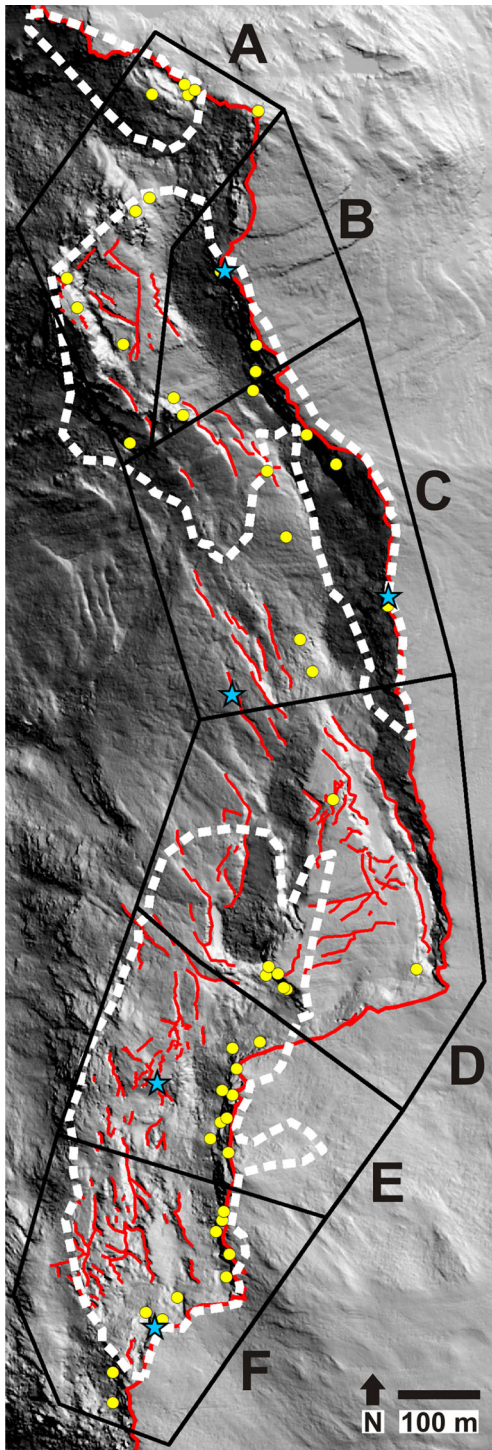
Fig. 2 Overview of data collected in zones A–F for kinematic and surface deformation analyses ("Structural measurements and kinematic analysis" and "Surface features, block volumes, and long-term movement rates" and Figs. 5 and 7). *Yellow points* denote locations of structural measurements, *blue stars* indicate TLS scan locations, and *white dashed lines* outline TLS coverage. *Red lines* indicate the main scarp, open cracks, and linear depressions measured on the airborne LiDAR. Extent of map is indicated by *white corner brackets* in Fig. 1.

was manually created, the mapping was guided by measurements of topographic curvature derived from a 2D wavelet transform of

the airborne LiDAR DEM (Booth et al. 2009), which highlighted meter-scale concave topographic features. To analyze the orientations of the mapped surface features, we broke the digitized features into segments at their vertices.

Results

InSAR movement rates

InSAR-derived deformation maps from 1992 to 2000 using the ERS-1 and ERS-2 satellites clearly show movement of at least several millimeters per year away from the satellite in the line-of-sight direction across the upper reaches of the Osmundneset landslide complex (Fig. 3a–c). Because the site's relative position is different within the image swaths from each of the three tracks, the look angle varies from ~19° from vertical for track 237, ~23° for track 008, and ~27° for track 280. The maximum line-of-sight velocity increases with incidence angle and is lowest for track 237 at ~3 mm year^{-1}, faster for track 008 at ~5 mm year^{-1}, and fastest for track 280 at ~8 mm year^{-1}. These velocities, which are all away from the satellite, suggest a general movement direction of down and to the west for most of the landslide complex including the two major blocks in the northern and central part of the site as well as the cracked ground in the southern part. Furthermore, the increase in line of site displacement rate with shallowing look angle suggests that movement of the landslide downward relative to the land surface slope dominates the signal.

In addition to the general pattern of movement throughout the landslide complex, the Radarsat-2 data reveal smaller scale variations in displacement rate within the landslide complex (Fig. 3d). For example, the fastest line-of-sight velocities of ~12 mm year^{-1} or more occur at the western edge of the region of cracked ground to the west of the central block and on the western face of the northern block. Moderate displacement rates of ~10 mm year^{-1} occupy the region between the central and northern blocks and the far southern part of the landslide complex. The lowest line-of-sight displacement rates occur on the top surfaces of the central and northern blocks as well as at the western margin of the cracked ground in the far southern part of the landslide complex.

dGNSS and dGPS movement vectors

All four roving points in the dGNSS/dGPS network showed statistically significant (with >99 % confidence) horizontal displacements generally to the west at rates of ~1 to 3 mm year^{-1} over the 4-year monitoring period (Table 1). Vertical displacements were not detectable at a statistically significant level. Points HY-1 and HY-2 at the southern end of the landslide complex both moved to the WNW by a total of 7.4±2.4 mm with a bearing of 316±18° and 10.0±2.1 mm with a bearing of 283±15°, respectively. Point HY-3 on the block in the center of the landslide complex moved a smaller distance of 4.9±1.9 mm with a bearing of 305±25°. Point HY-4 on the northern landslide block moved the farthest at 10.5±2.3 mm with a bearing of 234±13°.

Structural measurements and kinematic analysis

Hand and TLS-based structural measurements covered the full extent of the landslide complex where bedrock was exposed (Fig. 2) and documented three main structural features present throughout the site (Fig. 4). Two prominent sets of subvertical joints, which we designate j_1 and j_2, are found throughout the landslide complex, with
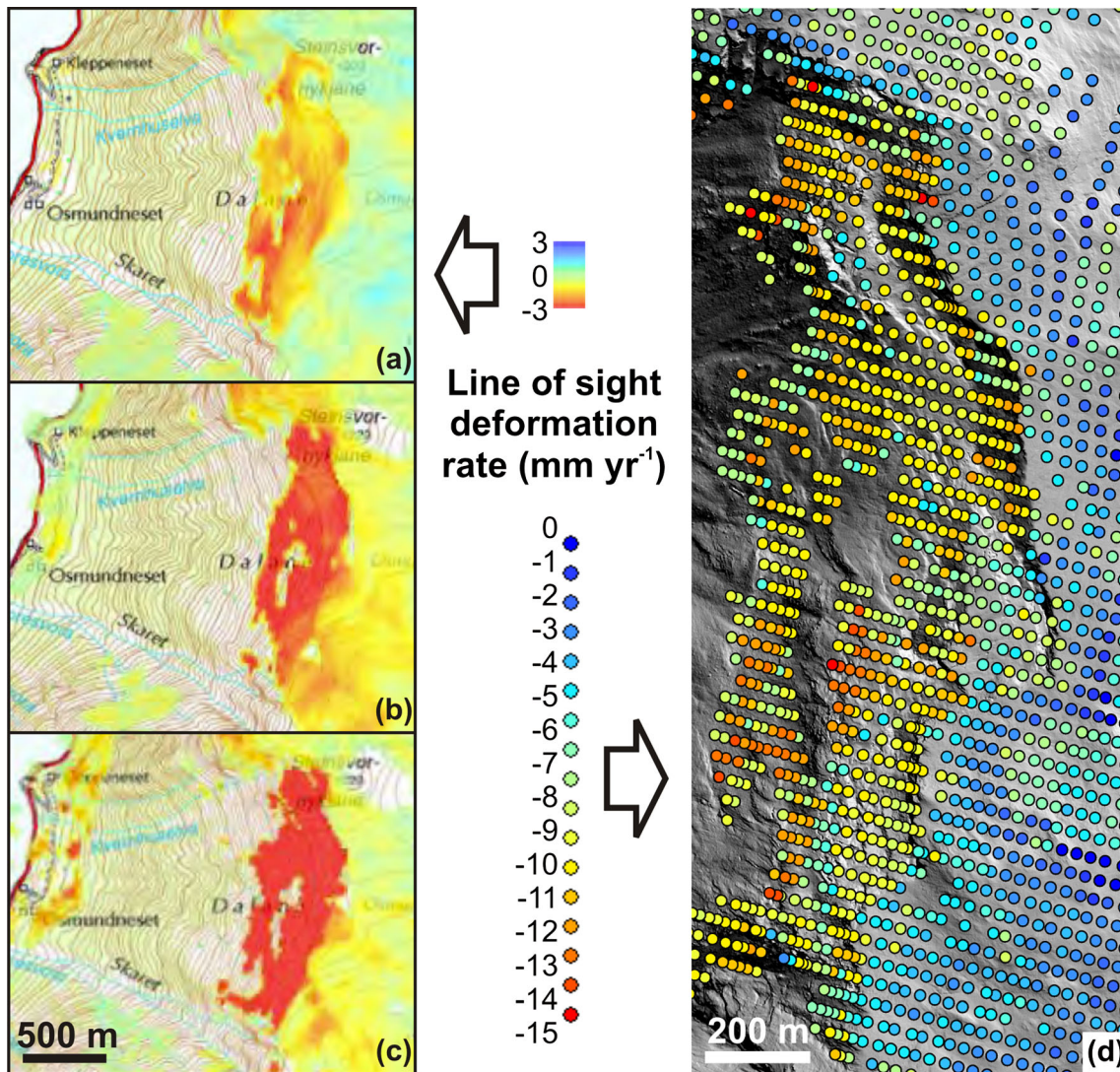
Fig. 3 InSAR-derived line-of-sight deformation fields at Osmundneset from 1992 to 2000 based on the ERS-1 and ERS-2 satellites (**a–c**) and for 2010–2013 from the Radarsat-2 satellite (**d**). Line of site direction is to the west with incidence angles of 19° (**a**), 23° (**b**), 27° (**c**), and 30° (**d**) from vertical

j_1 mainly dipping very steeply to the southwest and j_2 dipping steeply to the southeast. Measurements of j_1 tend to be tightly clustered at each measurement location with a subtle shift from dipping mainly northeast at the northern end of the site to dipping southwest at the southern end of the site (Fig. 4). Measurements of j_2 tend to be more scattered at a given measurement location and show no systematic shifts in dip or dip direction from place to place within the landslide complex. All three bedrock units present at the site are strongly foliated, and the foliation orientation changes from north to south across the landslide complex, as measurements traverse the broad synform with its axis near the center of the site. North of the axis, the foliation, fo, dips shallowly to the south; near the axis, the dip becomes more westward; and south of the axis, it becomes steeper and to the north.

Table 1 Differential GNSS-/GPS-derived displacements of the four roving monitoring points between 2008 and 2012. Reported uncertainties are $\pm3\sigma$ (99 % confidence) determined by standard Gaussian error propagation for the displacement magnitude and direction

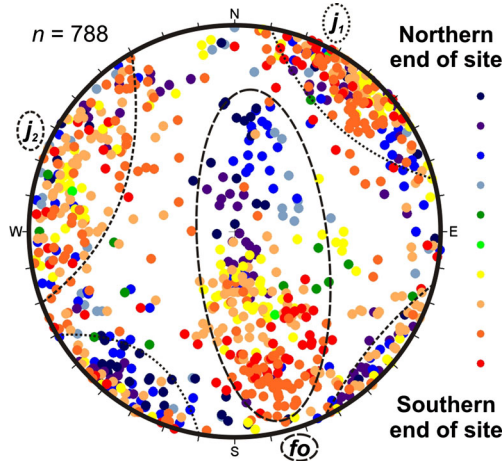| Point	x-displacement (mm)	y-displacement (mm)	Displacement magnitude (mm)	Displacement direction	Displacement rate (mm year^{-1})
HY-1	−5.1±2.1	5.3±2.5	7.4±2.4	316±18°	1.9±0.6
HY-2	−9.7±2.1	2.3±2.6	10.0±2.1	283±15°	2.4±0.5
HY-3	−4.0±1.7	2.8±2.3	4.9±1.9	305±25°	1.2±0.5
HY-4	−8.5±2.1	−6.1±2.6	10.5±2.3	234±13°	2.6±0.6

Fig. 4 Overview of structural orientations measured in the field and from TLS point clouds, color coded by northerly position within the landslide complex. Three *differently weighted dashed lines* outline the three major structural features present throughout the site, and the colors highlight changes in orientation of these features from north to south (j_1 and j_2=joints, fo=foliation)

Because of the spatially variable structural orientations, we subdivided the site into six zones, designated A–F from north to south, for further analysis (Figs. 2 and 5). We selected these zones using three criteria. First, the locations of the structural measurements included in a zone are close together in space so that they document the same basic surface feature of the landslide. For example, zone D includes all measurements on the central block. Second, within each zone, the mean orientations of each of the three documented rock structures are similar among all measurement locations. Third, each zone contains a minimum of 5 measurement locations, which amounts to at least 70 individual structural measurements. We conducted kinematic feasibility tests for planar or wedge sliding and toppling (Hoek and Bray 1981; Norrish and Wyllie 1996) in each of these six zones assuming no cohesion and a friction angle of 20°, which is typical for weathered discontinuities possibly containing gouge (Barton 1973; Wyllie and Mah 2004; Jaeger et al. 2009). Table 2 lists the mean orientations of structures and the topography used for the kinematic tests, and Fig. 5 illustrates the results for each zone indicated in Fig. 2.

In zone A, which includes the large block at the northern end of the landslide complex, a wedge failure mode is kinematically feasible and consists of sliding along the intersection of fo and j_2 with an orientation of 221°/20° (mean dip direction/dip) (Fig. 5a, Table 2). Additionally, some poles of j_1 plot in the toppling window, indicating that toppling to the southwest might also be an important failure mode within this zone. We therefore suggest a complex failure mode for this part of the landslide complex where the large block is likely translating to the southwest as a wedge failure while smaller rockfalls occur by toppling off of the block's steep face, creating a scree deposit (Fig. 6a).

In zone B, which consists of a near vertical rock wall up to 80 m in height (Fig. 6a) that defines the main scarp of the landslide to the east of zone A, none of the three kinematic failure modes are likely, although a few measured structures are locally prone to toppling (Fig. 5b). The foliation dips much less steeply than the assumed friction angle, which does not allow sliding or wedge failures. One

set of vertical joints, j_2, dips perpendicularly to the dip of the slope and is therefore not conducive to toppling, while the other set, j_1, tends to define the main cliff face and is locally susceptible to toppling where it dips steeply to the northeast into the main hillslope. These toppling failures are evident as a scree deposit below the cliff face (Fig. 6a), and the overall stability indicated by kinematic analysis is consistent with the observation that this rock wall marks the upslope extent of the landslide complex.

Zone C contains the central part of the landslide complex just north of the large central block, and both planar sliding on fo and toppling controlled by the vertical joints are kinematically feasible here (Fig. 5c). Because this zone is near the axis of the large synform, foliation dips moderately to the west, which allows sliding with mean dip direction/dip of 261°/25°. Both j_1 and j_2 have highly variable orientations here, which allow toppling over a wide range of directions from the northwest to the southwest. We therefore propose a combined failure mode in this zone consisting of sliding and domino-style flexural toppling with displacements generally to the west and southwest.

In zone D, which outlines the large central block, a wedge failure to the northwest on the intersection of fo and j_1 is the most likely kinematically feasible failure mode, with an orientation of 312°/20° (Fig. 5d). However, the orientations of a few fo measurements fall within the planar sliding window, and a few measurements of j_2 fall within the flexural toppling window, indicating that these modes might be possible locally where those structural orientations are present. The main block is displaced to the northwest of the main scarp in agreement with the wedge sliding orientation (Fig. 6b, c), and that is therefore most likely the dominant failure mode in this zone.

Structures in zone E have similar orientations to those in zone D, and a wedge failure on the intersection of fo and j_1 is again kinematically possible with an orientation of 306°/24° (Fig. 5e). Additionally, many orientations of j_2 fall within the flexural toppling window to the northwest, and planar sliding on fo is possible at a just few measurement locations. We propose a complex failure style at this location where flexural toppling, manifest as numerous open cracks exploiting j_1 and j_2 (Figure 6d), is likely accompanied by wedge sliding, both generally to the northwest.

Zone F contains the pervasively cracked ground at the southern end of the landslide complex, and flexural toppling on j_2 to the northwest is the only kinematically feasible failure mode there (Fig. 5f). This far away from the synform axis, fo, dips steeply to the north so that neither wedge nor planar sliding daylight on the subjacent slope. This implies that the numerous, large, and irregularly shaped cracks in this zone have resulted primarily from block-flexural toppling on j_2 below the main scarp (Fig. 6b).

At dGNSS/dGPS points HY-4, HY-3, HY-2, and HY-1, which lie in zones A, D, E, and F, respectively, the directions of movement inferred from the above kinematic tests agree with the horizontal displacement directions measured with dGNSS/dGPS. On the northern block in zone A, point HY-4 was displaced to the southwest in the direction 234±13° (Table 1), which compares to the 221° direction predicted for wedge sliding in this zone. This dGNSS/dGPS direction also falls within the toppling window predicted by the kinematic analysis, which does not rule out flexural toppling as providing a component of the measured displacement. At point HY-3 in zone D, movement measured using dGNSS/dGPS was to the northwest at 305±25°, which is in agreement with the 312°
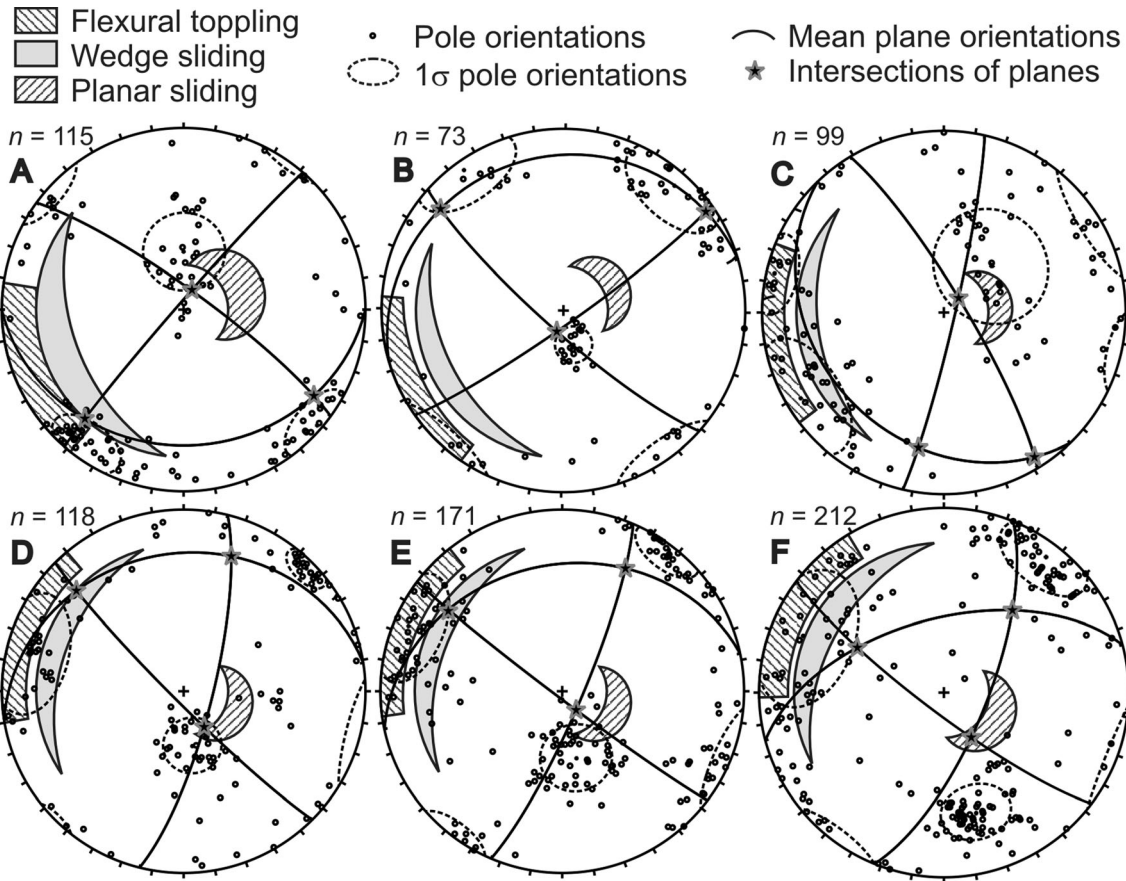
Fig. 5 Kinematic analyses for flexural toppling, wedge sliding, and planar sliding for zones A–F (Fig. 2). For toppling or planar sliding, pole orientations must plot in the relevant shaded window, and for wedge sliding, intersections of planes must plot in the shaded window for failure to be kinematically possible

orientation of a wedge failure of the large block in this zone. Because of the high uncertainty on the dGNSS-/dGPS-derived movement direction here, this observation is also consistent with planar sliding or flexural toppling to the northwest, although very few measured structures are oriented for these failure modes. At point HY-2 in zone E, where the landslide consists of pervasively cracked ground, the dGNSS/dGPS measurements indicate movement to the northwest at 283±15°, which is consistent with flexural toppling to the northwest in this zone. A few measured structural orientations would allow planar or wedge sliding to the northwest in this zone as well. Last, in zone F at point HY-1, the only kinematically feasible failure mode of toppling to the northwest agrees well with the dGNSS/dGPS movement

direction of 316±18°, confirming that it is most likely the dominant failure mechanism there.

Surface features, block volumes, and long-term movement rates

Using our map of surface cracks, scarps, trenches, and depressions (Fig. 2), we quantified the strike of these features in each of the six landslide zones (Fig. 7). At the northern end of the landslide complex (zones A and B), both j_1 and j_2 are expressed at the surface mainly as open cracks with decimeter to meter scale widths. Several 50-m or longer linear cracks as well as several step-path features of ~1 to 10 m in length follow these joint sets, especially on the surface and at the edges of the main large block. The main scarp also tends to be oriented along j_1 at the northern end of zone A and along j_2 on the eastern side of zone B where it defines the main scarp of the landslide complex. To the south in zone C, the surface features are mainly linear trenches or depressions that tend to follow the strike of j_1 or fo (Fig. 6c). Many of these trenches have uphill facing scarps consistent with planar sliding along fo, which is oriented subparallel to the hillslope surface in most of this zone (Table 1, Fig. 5). In zone D, many cracks and depressions are visible on and adjacent to the large displaced block (Fig. 6b), and the expressions of all three measured rock structures are clearly visible at the surface. Several linear depressions on the surface of the block and the main scarp to the south of the block tend to follow fo, while the surrounding cracks and the main scarp to the east of the block tend to follow j_1

Table 2 Mean slope orientation and the orientations of fo, j_1, and j_2 for zones A–F (Fig. 2) in the landslide complex. Notation is dip direction/dip

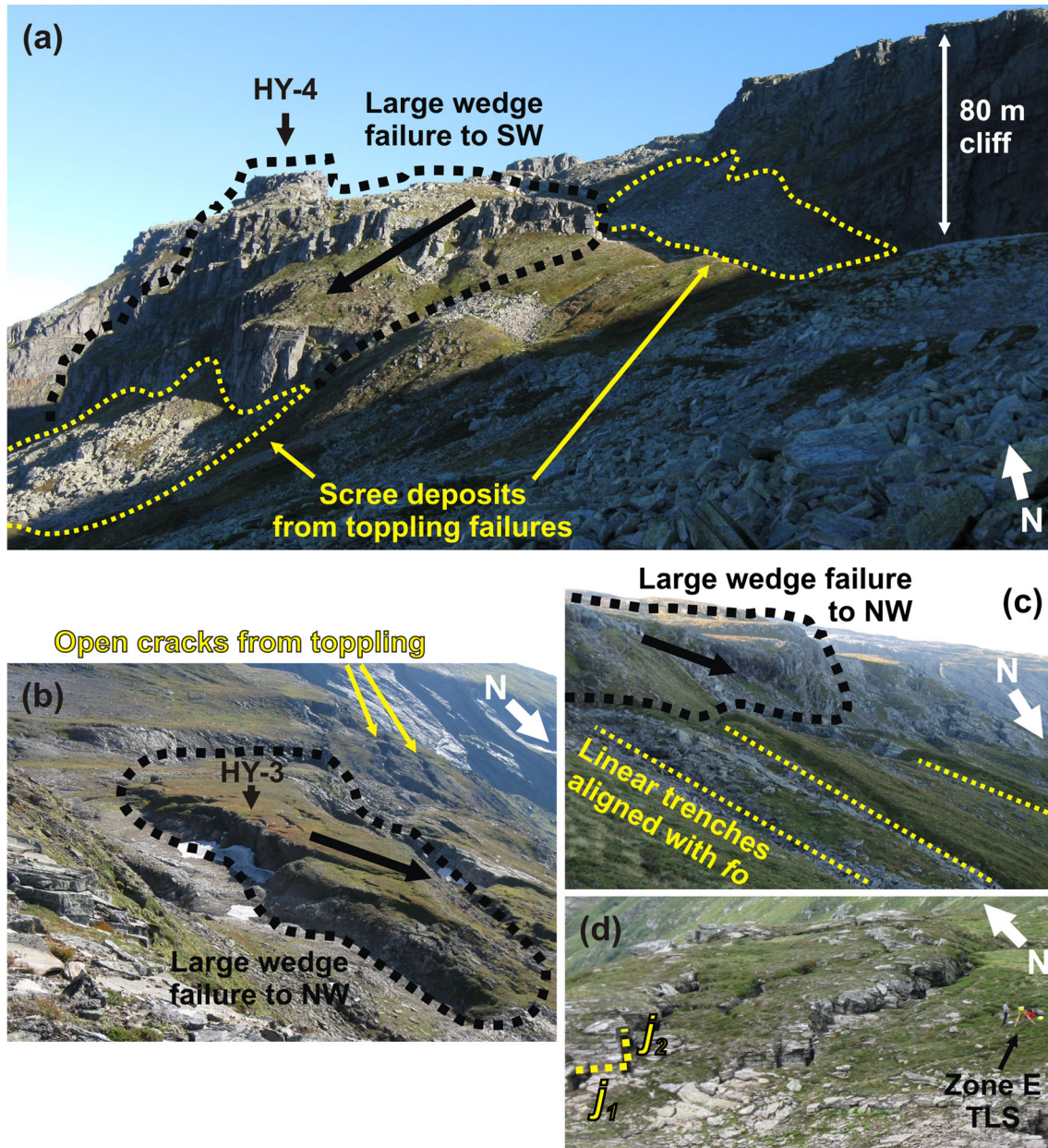| Zone	Slope	fo	j_1	j_2
A	249°/38°	180°/26°	036°/81°	315°/87°
B	242°/32°	343°/16°	221°/81°	146°/84°
C	262°/31°	225°/30°	060°/81°	099°/85°
D	290°/32°	351°/26°	225°/85°	101°/77°
E	291°/32°	348°/32°	225°/87°	111°/81°
F	299°/34°	345°/57°	216°/81°	110°/71°

Fig. 6 Photos illustrating failure modes and structures present in zones A and B (**a**), zones D, E, and F (**b**), zones C and D (**c**), and zone E (**d**). *Black outlines* indicate the northern and central blocks, *yellow lines* indicate other surface features, and *north arrows* and locations of dGNSS/dGPS or TLS survey points (Figs. 1 and 2) are given for orientation. Panel (**a**) shows the 1.5 million m^3 northern block which is translating to the southwest. Deposits of scree have accumulated in front of the block and in front of the main scarp due to small toppling failures. Panel (**b**) highlights the 1.7 million m^3 central block which is translating to the northwest as well as two large open cracks in the distance to the south resulting from complex block-flexural toppling. Panel (**c**) shows three linear trenches with uphill facing scarps formed by planar sliding on *fo* to the north of the large central block. Panel (**d**) highlights several open cracks that have exploited the two subvertical joint sets in a step-path pattern to accommodate motion to the northwest

or j_2. South of here in zones E and F, surface features are mainly large open cracks up to several meters in width with orientations that tend to be much more variable than in other zones (Fig. 6b, d). Although there is a less clear correspondence between these surface features and measured structural orientations, the surface cracks broadly tend to be oriented in a north–south direction that parallels the main scarp, suggesting that they are exploiting a combination of j_1 and j_2 with numerous step-overs from one joint set to the other (Fig. 6d).

We also used the surface feature map to aid in delineating the two large, displaced blocks in zones A and D in order to estimate their volumes. Additional smaller blocks are present throughout the rest of the landslide complex, but these blocks are mostly moving by flexural toppling, and we do not have a good enough estimate of their depths to determine their volumes. For the northern and central blocks, we differenced the airborne LiDAR DEM and an interpolated DEM that was created from a tensioned spline fit (Wessel and Bercovici 1998) to the surface surrounding

Fig. 7 Rose diagrams showing relative frequency of the main scarp, surface cracks, ▶
trenches, and linear depression orientations for landslide zones A–F (Fig. 2).
Surface feature orientations that clearly align with the strike of rock structure
orientations (Fig. 5) are indicated with *fo*, *j₁*, or *j₂*

each block (Fig. 8). The upslope margin of each block was defined
as the base of the main scarp of the landslide complex, and the
downslope extent of each block was inferred to occur at the first
major break in slope below each block's front face. This estimation
of the downslope extent is somewhat equivocal and represents a
source of uncertainty in determining each block's volume since we
do not find reliable indicators of the failure plane, such as springs
or convex bulges in the hillslope, below either block. For the spline
fit, a very light normalized tension parameter of 0.01 (Wessel and
Bercovici 1998) resulted in a smooth interpolated surface that also
captured the more abrupt change in slope between the main scarp
and the hillslope below (Fig. 8). Given these assumptions, the
northern block has a volume of 1.5 million m³ and a maximum
thickness of 60 m, while the central block is slightly larger and
thinner with a volume of 1.7 million m³ and a maximum thickness
of 50 m.

Both these blocks are clearly displaced from the main scarp
indicating that the millimeter to centimeter scale displacements
measured with the dGNSS/dGPS campaign are only a small part of
the total block movement over a longer time period. The precise
timing of landslide initiation is unknown, but seismic activity,
hydrologic conditions, glacial debutressing, and frost-related pro-
cesses can all trigger bedrock landslides in western Norway
(Braathen et al. 2004; Blikra et al. 2006). Therefore, the earliest
the landslide likely initiated is ~12 k.a. following debutressing
caused by the retreat of the valley glacier (Mangerud et al. 1979).
We measure a total displacement of 102±16 m (mean±99 % con-
fidence interval) for the northern block which, assuming initiation
at 12 k.a., gives a minimum Holocene average displacement rate of
8.5±1.4 mm year⁻¹. This is greater than the dGNSS-/dGPS-derived
short-term displacement rate of point HY-4 implying that this
block is currently moving more slowly than the long-term average.
For the central block, the total Holocene displacement is 28±5 m
giving a minimum rate of 2.3±0.4 mm year⁻¹, which is statistically
indistinguishable from the modern dGNSS-/dGPS-derived rate of
point HY-3 and suggests continued slow, steady displacement
through the Holocene.

Discussion and qualitative hazard assessment

Our synthesis of InSAR, dGNSS/dGPS, structural, and geomorphic
data allows us to thoroughly document the failure mechanisms
and rates of movement throughout the landslide complex, provid-
ing a basis to estimate the landslide's future behavior. Since the
two large blocks have volumes comparable to landslides that
historically caused more than 100 deaths in the nearby inner fjord
settings of Loen and Tafjord (Jørstad 1968), two important ques-
tions are whether either of these blocks will fail catastrophically
and what the consequences would be. We discuss the possibilities
below in the context of a qualitative risk classification scheme for
rock slopes in Norway (Hermanns et al. 2013b). In the classifica-
tion scheme, each of the following nine observations indicates a
relatively higher hazard: a well-developed scarp, steeply dipping
structures that daylight on the slope, the presence of lateral release
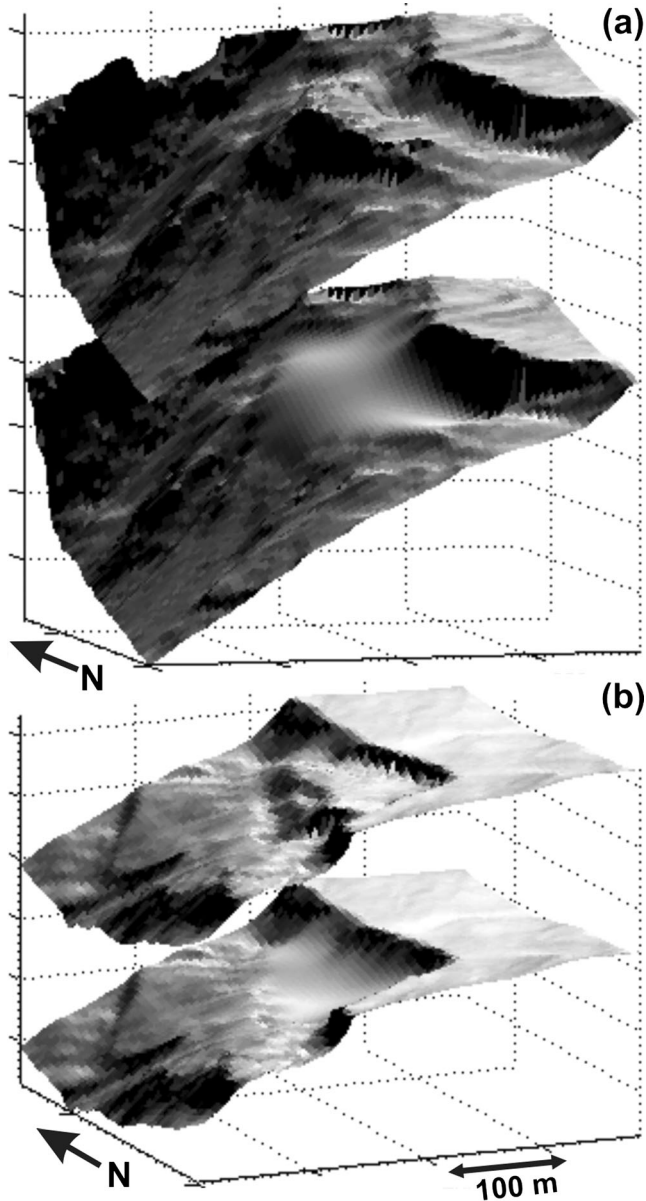structures, kinematic feasibility tests that indicate planar sliding,
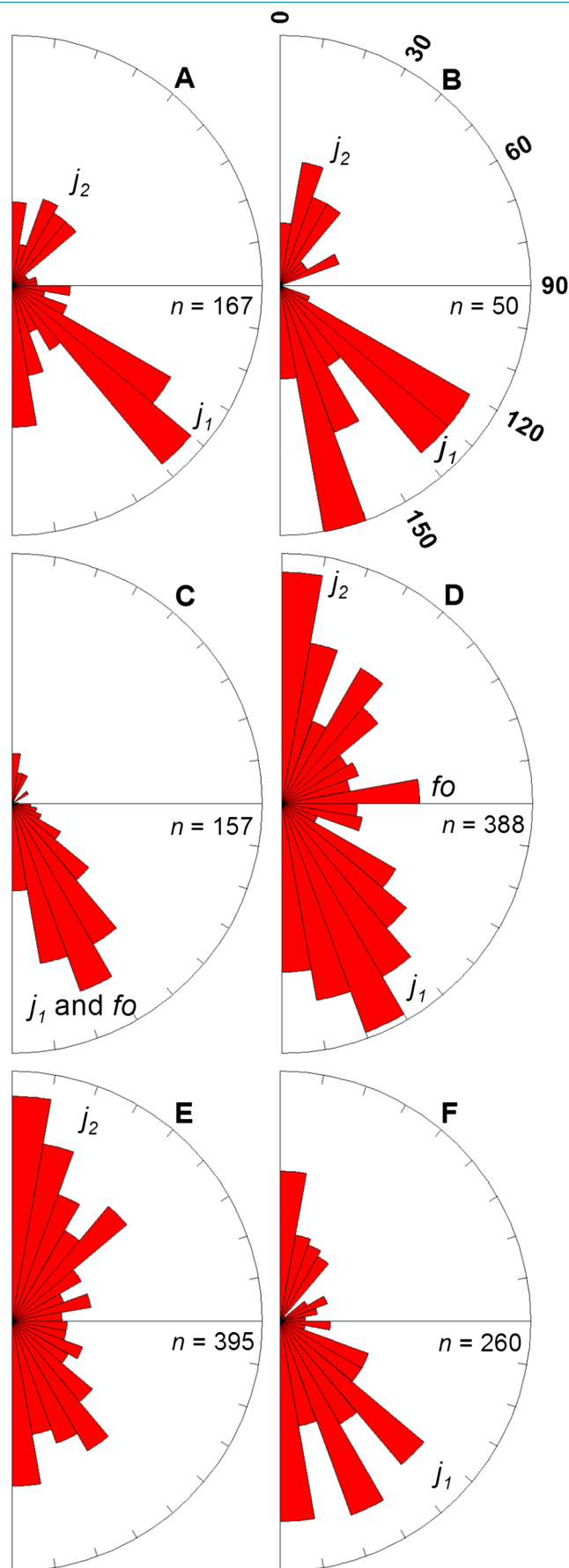
Fig. 8 Interpolated surfaces (*lower*) and actual surfaces (*upper*) used to estimate volumes of the northern (**a**) and central (**b**) blocks. *Horizontal* and *vertical grid* spacing is 100 m and view angle is to the NE. *Shading* is the magnitude of the topographic gradient

wedge sliding, or toppling, morphologic expression of the rupture surface, more rapid displacement rates, accelerating displacement rates, increasing rockfall activity, and evidence of past rock avalanche events.

The Osmundneset landslide complex has several well-developed features that point to a potential hazard in this classification scheme. First, there is a clearly defined main scarp extending the full ~1.8-km length of the landslide complex (Fig. 2) which indicates that a large amount of rock has been displaced away from the scarp by as much as ~100 m ("Surface features, block volumes, and long-term movement rates"). Second, throughout the landslide complex, there are persistent discontinuities with orientations that have allowed these displacements to take place by complex deformation mechanisms

including combinations of planar sliding, wedge sliding, and forward toppling (Fig. 5). These structures remain oriented to allow future landslide movement. Third, the two large blocks have reasonably well-defined lateral margins (Figs. 1d, 6a, b, and 8) that indicate they have translated somewhat coherently for tens to hundreds of meters, rather than breaking apart into smaller subblocks. However, several other characteristics at Osmundneset indicate a lower relative hazard. The surfaces of the large blocks are presently riddled with open cracks and linear depressions, suggesting that the pattern of coherent translation might not continue and instead, the smaller subblocks could detach independently. The average displacement rate of ~2 mm year^{-1} (Table 1) for the four points in the dGNSS/dGPS monitoring network are slow relative to rates on the order of a centimeter per year measured at other sites in Norway (Ganerød et al. 2008; Hermanns et al. 2011; Kristensen and Blikra 2013), indicating a lower hazard relative to these sites. Furthermore, both large blocks are currently moving at rates similar to or slower than their long-term rates averaged over the Holocene. Although this steady or decelerating motion does not rule out eventual catastrophic failure, the landslide complex does not appear to be accelerating toward rapid failure at this time. Finally, there are no rock avalanche deposits visible in the fjord bathymetry (Hermanns et al. 2011), which suggests no catastrophic failures have occurred here during the Holocene. Taken together, these observations suggest a low to medium qualitative hazard classification (Hermanns et al. 2013b).

Despite the low or moderate hazard presented by the landslide complex, the consequences of a large, catastrophic failure could be devastating to local communities because of the landslide's position high above Hyenfjord. Since the largest blocks have volumes on the order of 10^6 m³, it is reasonable to assume that large parts or the entirety of these blocks would run-out down the steep hillslope and enter the fjord at high speed (Scheidegger 1973; Hsü 1978; Davies and McSaveney 2002), causing a displacement wave as occurred historically in other nearby fjords. The historical tsunamis in Loen and Tafjord reached heights of several to tens of meters above the shoreline at locations several kilometers from the rock avalanche site (Jørstad 1968). At Osmundneset, several farms immediately below the landslide complex would likely be affected as well as the numerous small coastal communities mainly to the south. We therefore estimate a moderate potential loss of 10 to 100 lives, which places it in the moderate risk category for unstable rock slopes in Norway when combined with the low to medium hazard estimated above (Hermanns et al. 2013b).

Conclusions

This paper presents a synthesis of geologic and geodetic data to thoroughly document the spatial pattern of movement rates and failure mechanisms at the Osmundneset landslide complex, Sogn og Fjordane province, Norway. We first discovered this landslide complex by systematic InSAR reconnaissance, which reveals movement at rates on the order of millimeters per year away from the satellite in the line-of-sight direction (down and to the west) over an ~1.8-km-long section of the eastern slope of Hyenfjord. A dGNSS/dGPS campaign begun in 2008 confirms active deformation with horizontal displacement rates of 1.2 to 2.6 mm year^{-1} at four points distributed across the landslide. The dGNSS/dGPS movement directions are consistent with landslide displacements occurring on pre-existing discontinuity sets, documented with a combination of hand and TLS-based structural orientation

measurements. A broad fold in the foliated bedrock controls the failure mechanism within the landslide complex. Two large blocks with volumes on the order of 10^6 m³ are likely wedge failures on the intersection of foliation planes and subvertical tectonic fractures, while flexural toppling and planar sliding of smaller blocks is possible throughout the landslide complex. The dGNSS-/dGPS-derived movement rates are comparable to or slower than Holocene-averaged minimum displacement rates, suggesting continued steady deformation or stabilization of parts of the landslide with time. However, a large, rapid failure would likely cause a displacement wave in the fjord below and result in loss of lives, so we qualitatively assign a moderate risk to the site. The collaborative approach of integrating a wide variety of geologic and geodetic methods will be useful for more thoroughly documenting additional landslide sites and for making informed decisions about risk management.

References

Abellán A, Vilaplana J, Martínez J (2006) Application of a long-range terrestrial laser scanner to a detailed rockfall study at vall de núria (eastern Pyrenees, Spain). Eng Geol 88:136–148

Barton N (1973) Review of a new shear-strength criterion for rock joints. Eng Geol 7:287–332

Bjerrum L, Jørstad F (1968) Stability of rock slopes in Norway. Technical Reports, Norwegian Geotechnical Institute, Oslo, pp 1–11

Blikra L, Longva O, Harbitz C, Løvholt F (2005) Quantification of rock-avalanche and tsunami hazard in Storfjorden, Western Norway. Landslides and Avalanches ICFL: 57–64

Blikra L, Longva O, Braathen A, Anda E, Dehls J, Stalsberg K (2006) Rock slope failures in Norwegian fjord areas: examples, spatial distribution and temporal pattern. Landslides from massive rock slope failure. Springer, pp 475–496

Böhme M, Saintot A, Henderson IH, Henriksen H, Hermanns RL (2011) Rock slope instabilities in Sogn and Fjordane county, Norway: a detailed structural and geomorphological analysis. Geol Soc Lond, Spec Publ 351:97–111

Booth AM, Roering JJ, Perron JT (2009) Automated landslide mapping using spectral analysis and high-resolution topographic data: Puget Sound lowlands, Washington, and Portland Hills, Oregon. Geomorphology 109:132–147. doi:10.1016/j.geomorph.2009.02.027

Bornhold BD, Harper JR, McLaren D, Thomson RE (2007) Destruction of the first nations village of Kwalate by a rock avalanche–generated tsunami. Atmosphere-Ocean 45:123–128. doi:10.3137/ao.450205

Braathen A, Blikra LH, Berg SS, Karlsen F (2004) Rock-slope failures of Norway, type, geometry deformation mechanisms and stability. Nor Geol Tidsskr 84:67–88

Brideau M-A, Stead D, Kinakin D, Fecova K (2005) Influence of tectonic structures on the Hope Slide, British Columbia, Canada. Eng Geol 80:242–259. doi:10.1016/j.enggeo.2005.05.004

Brideau M-A, Stead D, Couture R (2006) Structural and engineering geology of the east gate landslide, Purcell Mountains, British Columbia, Canada. Eng Geol 84:183–206. doi:10.1016/j.enggeo.2006.01.004

Bryhni I (2000) Bedrock map Nordfjordeid 1218 i. Norw Geol Surv, Oslo

Crosta G, Agliardi F (2003) Failure forecast for large rock slides by surface displacement measurements. Can Geotech J 40:176–191

Cruden D (1976) Major rock slides in the rockies. Can Geotech J 13:8–20

Davies TR, McSaveney MJ (2002) Dynamic simulation of the motion of fragmenting rock avalanches. Can Geotech J 39:789–798. doi:10.1139/t02-035

Evans SG (1989) The 1946 Mount Colonel Foster rock avalanche and associated displacement wave, Vancouver Island, British Columbia. Can Geotech J 26:447–452

Evans S, Clague J (1988) Catastrophic rock avalanches in glacial environments. Proceedings of the 5th International Symposium on Landslides, pp 1153–1158

Evans SG, DeGraff JV (2002) Catastrophic landslides: effects, occurrence, and mechanisms. Geological Society of America, Boulder

Evans SG, Hermanns RL, Strom AL, Scarascia-Mugnozza G (2011) Natural and artifical rockslide dams. Springer, New York

Feng QH, Röshoff K (2004) In-situ mapping and documentation of rock faces using a full-coverage 3d laser scanning technique. Int J Rock Mech Min Sci 41(Supplement 1):139–144. doi:10.1016/j.ijrmms.2004.03.032

Ferrero A, Forlani G, Roncella R, Voyat H (2009) Advanced geostructural survey methods applied to rock mass characterization. Rock Mech Rock Eng 42:631–665

Ganerød GV, Grøneng G, Rønning JS, Dalsegg E, Elvebakk H, Tønnesen JF, Kveldsvik V, Eiken T, Blikra LH, Braathen A (2008) Geological model of the Åknes rockslide, western Norway. Eng Geol 102:1–18. doi:10.1016/j.enggeo.2008.01.018

Grimstad E, Nesdal S (1990) The Loen rockslides—a historical review. In: Barton M, Stephansson W (eds) Rock Joints: Proceedings of the International Symposium on Rock Joints, Loen, Norway, 4–6 June, 1990, A.A. Balkema, pp 3–8

Henderson IH, Saintot A (2011) Regional spatial variations in rockslide distribution from structural geology ranking: an example from Storfjorden, western Norway. Geol Soc Lond, Spec Publ 351:79–95

Henderson I, Saintot A, Böhme M, Henriksen H (2008) Kartlegging av mulig ustabile fjellpartier, Sogn og Fjordane. Norges geologiske undersøkelse Report

Hendron AJ, Patton FD (1987) The Vaiont slide—a geotechnical analysis based on new geologic observations of the failure surface. Eng Geol 24:475–491. doi:10.1016/0013-7952(87)90080-9

Hermanns RL, Strecker MR (1999) Structural and lithological controls on large Quaternary rock avalanches (sturzstroms) in arid northwestern Argentina. Geol Soc Am Bull 111:934–948. doi:10.1130/0016-7606(1999)111<0934:salcol>2.3.co;2

Hermanns R, Niedermann S, Ivy-Ochs S, Kubik P (2004) Rock avalanching into a landslide-dammed lake causing multiple dam failure in Las Conchas valley (NW Argentina): evidence from surface exposure dating and stratigraphic analyses. Landslides 1. doi:10.1007/s10346-004-0013-5

Hermanns RL, Blikra LH, Naumann M, Nilsen B, Panthi KK, Stromeyer D, Longva O (2006) Examples of multiple rock-slope collapses from Köfels (Ötz valley, Austria) and western Norway. Eng Geol 83:94–108. doi:10.1016/j.enggeo.2005.06.026

Hermanns RL, Fischer L, Oppikofer T, Bøhme M, Dehls J, Henriksen H, Booth AM, Longva O, Eilertsen R, Eiken T (2011) Mapping of unstable and potentially unstable slopes in Sogne og Fjordane (work report 2008–2010). Norges Geologiske Undersøkelse

Hermanns RL, Blikra LH, Anda E, Saintot A, Dahle H, Oppikofer T, Fischer L, Bunkholt H, Böhme M, Dehls JF (2013a) Systematic mapping of large unstable rock slopes in Norway. Landslide science and practice, Springer, pp 29–34

Hermanns RL, Oppikofer T, Anda E, Blikra LH, Böhme M, Bunkholt H, Crosta GB, Dahle H, Devoli G, Fischer L (2013b) Hazard and risk classification for large unstable rock slopes in Norway. Ital J Eng Geol Environ. doi:10.4408/IJEGE.2013-06.B-22

Hewitt K, Clague JJ, Orwin JF (2008) Legacies of catastrophic rock slope failures in mountain landscapes. Earth Sci Rev 87:1–38. doi:10.1016/j.earscirev.2007.10.002

Hoek E, Bray J (1981) Rock slope engineering. Taylor & Francis, London

Høst J (2006) Store fjellskred i Norge. Utredning for LMD på vegne av 6

Hsü K (1978) Albert heim: observations on landslides and relevance to modern interpretations. Rockslides Avalanches 1:71–93

Jaboyedoff M, Crosta GB, Stead D (2011a) Slope tectonics: a short introduction. Geol Soc Lond, Spec Publ 351:1–10. doi:10.1144/sp351.1

Jaboyedoff M, Oppikofer T, Derron M-H, Blikra LH, Böhme M, Saintot A (2011b) Complex landslide behaviour and structural control: a three-dimensional conceptual model of Åknes rockslide, Norway. Geol Soc Lond, Spec Publ 351:147–161

Jaeger JC, Cook NG, Zimmerman R (2009) Fundamentals of rock mechanics. Wiley, New York

Jørstad F (1968) Waves generated by landslides in Norwegian fjords and lakes. Technical Reports, Norwegian Geotechnical Institute, Oslo, pp 13–32

Kilburn CRJ, Petley DN (2003) Forecasting giant, catastrophic slope collapse: lessons from Vajont, northern Italy. Geomorphology 54:21–32. doi:10.1016/s0169-555x(03)00052-7

Korup O, Clague JJ, Hermanns RL, Hewitt K, Strom AL, Weidinger JT (2007) Giant landslides, topography, and erosion. Earth Planet Sci Lett 261:578–589. doi:10.1016/j.epsl.2007.07.025

Korup O, Densmore AL, Schlunegger F (2010) The role of landslides in mountain range evolution. Geomorphology 120:77–90. doi:10.1016/j.geomorph.2009.09.017

Kremer K, Marillier F, Hilbe M, Simpson G, Dupuy D, Yrro BJF, Rachoud-Schneider A-M, Corboud P, Bellwald B, Wildi W, Girardclos S (2014) Lake dwellers occupation gap in Lake Geneva (France–Switzerland) possibly explained by an earthquake–mass movement–tsunami event during early bronze age. Earth Planet Sci Lett 385:28–39. doi:10.1016/j.epsl.2013.09.017

Kristensen L, Blikra LH (2013) Monitoring displacement on the Mannen rockslide in western Norway. Landslide science and practice. Springer, pp 251–256

Larsen Y, Engen G, Lauknes TR, Malnes E, Høgda KA (2006) A generic differential interferometric SAR processing system, with applications to land subsidence and snow-water equivalent retrieval. Fringe 2005 Workshop, pp 56

Lauknes TR, Zebker HA, Larsen Y (2011) Insar deformation time series using an l1-norm small-baseline approach. IEEE Trans Geosci Remote Sens 49:536–546

Mangerud J, Larsen E, Longva O, Sønstegaard E (1979) Glacial history of western Norway 15,000–10,000bp. Boreas 8:179–187

McSaveney M (2002) Recent rockfalls and rock avalanches in Mount Cook national park, New Zealand. In: Evans SG, De Graff JV (eds) Catastrophic landslides: effects, occurrence, and mechanisms. Geological Society of America, Boulder, pp 35–70

Norrish NI, Wyllie DC (1996) Rock slope stability analysis. Landslides Investigation Mitigation Special Report 247:391–425

Oppikofer T, Jaboyedoff M, Blikra L, Derron M-H, Metzger R (2009) Characterization and monitoring of the Åknes rockslide using terrestrial laser scanning. Nat Hazards Earth Syst Sci 9:1003–1019

Oppikofer T, Jaboyedoff M, Pedrazzini A, Derron M-H, Blikra LH (2011) Detailed dem analysis of a rockslide scar to characterize the basal sliding surface of active rockslides. J Geophys Res 116. doi:10.1029/2010jf001807

Plafker G, Ericksen G (1978) Nevados Huascaran avalanches, Peru. Rockslides Avalanches 1:277–314

Redfield TF, Osmundsen PT (2009) The tjellefonna fault system of western Norway: linking late-Caledonian extension, post-Caledonian normal faulting, and tertiary rock column uplift with the landslide-generated tsunami event of 1756. Tectonophysics 474:106–123. doi:10.1016/j.tecto.2009.02.006

Saintot A, Henderson I, Derron M-H (2011) Inheritance of ductile and brittle structures in the development of large rock slope instabilities: examples from western Norway. Geol Soc Lond, Spec Publ 351:27–78

Saintot A, Oppikofer T, Derron M-H (2012) Large gravitational rock slope deformation in Romsdalen valley (western Norway). Rev Asoc Geol Argent 69:354–371

Sartori M, Baillifard F, Jaboyedoff M, Rouiller J-D (2003) Kinematics of the 1991 Randa Rockslides (Valais, Switzerland). Nat Hazards Earth Syst Sci 3:423–433

Scheidegger AE (1973) On the prediction of the reach and velocity of catastrophic landslides. Rock Mech 5:231–236

Schuster RL, Logan RL, Pringle PT (1992) Prehistoric rock avalanches in the Olympic Mountains, Washington. Science 258:1620–1620

Sturzenegger M, Stead D (2009a) Close-range terrestrial digital photogrammetry and terrestrial laser scanning for discontinuity characterization on rock cuts. Eng Geol 106:163–182

Sturzenegger M, Stead D (2009b) Quantifying discontinuity orientation and persistence on high mountain rock slopes and large landslides using terrestrial remote sensing techniques. Nat Hazards Earth Syst Sci 9:267–287

Voight B (1989) A relation to describe rate-dependent material failure. Science 243:200–203. doi:10.2307/1702921

Wessel P, Bercovici D (1998) Interpolation with splines in tension: a Green's function approach. Math Geol 30:77–93. doi:10.1023/A:1021713421882

Whitehouse IE (1983) Distribution of large rock avalanche deposits in the central southern alps, New Zealand. N Z J Geol Geophys 26:271–279

Wyllie DC, Mah C (2004) Rock slope engineering. Taylor & Francis, London

A. M. Booth (✉)
Department of Geology,
Portland State University,
17 Cramer Hall, 1721 SW Broadway, Portland, OR 97201, USA
e-mail: boothad@pdx.edu

J. Dehls · L. Fischer · R. L. Hermanns · T. Oppikofer
Geological Survey of Norway,
P.O. Box 6315 Sluppen, 7491, Trondheim, Norway

T. Eiken
Department of Geosciences,
University of Oslo,
Post Box 1047 Blindern, 0316, Oslo, Norway